

Nanoscale

Accepted Manuscript



This is an *Accepted Manuscript*, which has been through the Royal Society of Chemistry peer review process and has been accepted for publication.

Accepted Manuscripts are published online shortly after acceptance, before technical editing, formatting and proof reading. Using this free service, authors can make their results available to the community, in citable form, before we publish the edited article. We will replace this *Accepted Manuscript* with the edited and formatted *Advance Article* as soon as it is available.

You can find more information about *Accepted Manuscripts* in the [Information for Authors](#).

Please note that technical editing may introduce minor changes to the text and/or graphics, which may alter content. The journal's standard [Terms & Conditions](#) and the [Ethical guidelines](#) still apply. In no event shall the Royal Society of Chemistry be held responsible for any errors or omissions in this *Accepted Manuscript* or any consequences arising from the use of any information it contains.



Journal Name

ARTICLE

Influence of I/Cl ratio on the performance of $\text{CH}_3\text{NH}_3\text{PbI}_{3-x}\text{Cl}_x$ -based solar cells: why is $\text{CH}_3\text{NH}_3\text{I}:\text{PbCl}_2=3:1$ the “magic” ratio?

John A. McLeod,^{a,b} Zhongwei Wu,^a Baoquan Sun^{*a} and Lijia Liu^{*a,b}Received 00th January 20xx,
Accepted 00th January 20xx

DOI: 10.1039/x0xx00000x

www.rsc.org/

Methylammonium lead trihalide ($\text{CH}_3\text{NH}_3\text{PbI}_{3-x}\text{Cl}_x$) perovskite is usually synthesized from two precursors, $\text{CH}_3\text{NH}_3\text{I}$ and PbCl_2 at a ratio of 3:1. It was found that the slight adjustment of I/Cl ratio in the precursor mixture plays a strong effect on solar cell performance. In this study, perovskites made with different I/Cl ratios were comparatively studied. In combination with X-ray diffraction (XRD) and X-ray absorption fine structure (XAFS) measured at the Pb L₃-edge, we demonstrate that the device performance can be directly correlated to the change in the coordination environment of Pb

Introduction

Methylammonium lead trihalide perovskites $\text{CH}_3\text{NH}_3\text{PbX}_3$ (X=I, Br, Cl) has become a new class of light absorbing material in photovoltaic device fabrication. They can be easily synthesized by solution chemistry with relatively low cost, and upon incorporating into solar cells, the devices have demonstrated high power conversion efficiencies.¹⁻³ In the $\text{CH}_3\text{NH}_3\text{PbX}_3$ family, a mixed halide containing both I and Cl, namely $\text{CH}_3\text{NH}_3\text{PbI}_{3-x}\text{Cl}_x$ has demonstrated extra-long carrier diffusion length with drastically improved device performance.^{4,5} $\text{CH}_3\text{NH}_3\text{PbI}_{3-x}\text{Cl}_x$ is synthesized from a $\text{CH}_3\text{NH}_3\text{I}$ and PbCl_2 blend according to a common recipe,^{3,7} in which the ratio of $\text{CH}_3\text{NH}_3\text{I}$ and PbCl_2 is optimized to 3:1. Although the device performance is significantly improved by using mixed I-Cl halide perovskite than triiodide perovskite for one-step film fabrication process, $\text{CH}_3\text{NH}_3\text{PbI}_{3-x}\text{Cl}_x$ is found to possess an almost identical crystal structure and electronic structure as $\text{CH}_3\text{NH}_3\text{PbI}_3$, as evidenced by X-ray diffraction (XRD) and X-ray photoelectron spectroscopy (XPS).^{3, 8-10} In particular, no Cl (or only trace amount) was detected in any of the element-specific spectroscopy techniques, including laboratory and hard X-ray XPS, as well as bulk sensitive energy dispersive spectrometry (EDS).⁸⁻¹²

This brings up an interesting yet important question. Why does a perovskite synthesized from two halide sources exhibits the same structure, but a greatly improved photovoltaic performance, as the one made from a single halide? Many studies have been carried out to investigate the role of Cl in perovskite formation.¹¹⁻¹⁷ A widely accepted opinion is the introduction of Cl is beneficial to the process of perovskite

formation for photovoltaics (i.e. possibly resulting in better crystallinity), even though Cl may not remain in the perovskite lattice.^{8,15,17} Meanwhile, a recent study demonstrated that even for films of similar morphologies, deliberately adding Cl leads to a better device, so the authors attribute the role of Cl is to improve the charge transport at the interface.⁹ One open question is noteworthy. The widely used solution-based synthesis of perovskite is by mixing appropriate $\text{CH}_3\text{NH}_3\text{X}$ and PbX_2 at a certain ratio. For triiodide, there is no doubt that a $\text{CH}_3\text{NH}_3\text{I}:\text{PbI}_2$ 1:1 produces $\text{CH}_3\text{NH}_3\text{PbI}_3$ according to the stoichiometry. For a Br/I mixture, the I/Br ratio can be made flexible, and the resulted perovskite has a tunable electronic and optical properties.¹⁸ The mixed I/Cl perovskite, however, only works well when the organic and inorganic precursors has a ratio of 3:1.¹³ Although the limited solubility of $\text{CH}_3\text{NH}_3\text{I}$ and PbCl_2 makes tuning Cl concentration over the entire spectrum less flexible,^{13,19} within the window that the two precursors are both soluble, a 3:1 seems to be a “magic” number.

The reaction mechanism proposed for $\text{CH}_3\text{NH}_3\text{PbI}_{3-x}\text{Cl}_x$ formation^{16,20} is



The $\text{CH}_3\text{NH}_3\text{Cl}$ by-product is volatile and can easily escape from the film during annealing, which agrees with the characterization results that Cl was barely found in the final product.⁸ Since there is only trace amount (if any) of Cl present in the perovskite final product, $\text{CH}_3\text{NH}_3\text{PbI}_{3-x}\text{Cl}_x$ can be instead expressed as $\text{CH}_3\text{NH}_3\text{PbI}_3$. Meanwhile, the formation of various intermediate phases such as $\text{CH}_3\text{NH}_3\text{Cl}$ and $\text{CH}_3\text{NH}_3\text{PbCl}_3$ have also been proposed.^{15,16}

To confirm whether the reaction proceeds as the equation listed above, it is desirable to have a better understanding of the structure of the final product. This requires characterization techniques that could provide accurate local structures of the product formed throughout the perovskite film. The commonly used characterization techniques are XRD and XPS, but each has its limitation. For example, $\text{CH}_3\text{NH}_3\text{PbI}_3$

^a Jiangsu Key Laboratory for Carbon-based Materials and Devices, Institute of Functional Nano and Soft Materials (FUNSOM), Soochow University, Suzhou, Jiangsu 215123 China Email: bqsun@suda.edu.cn; ljlju@suda.edu.cn

^b Soochow University-Western University Centre for Synchrotron Radiation Research, Soochow University, Suzhou, Jiangsu 215123 China

$x\text{Cl}_x$, regardless of the Cl content and the preparation method, is usually identified by two or three diffraction peaks, which are assigned to the (110), (220) and (310) (if present) of a tetragonal lattice.^{7,10,21,22} $\text{CH}_3\text{NH}_3\text{PbI}_3$, however, also often exhibits multiple diffraction peaks, especially in the form of a single crystal.²³ In most cases, a tetragonal perovskite crystal structures are identified in the literature based on the identification of the (110) and (220) peaks, and other weak diffraction peaks are often not discussed during the data analysis.^{7,10,21,22} With only a few peaks, a full Rietveld refinement of these XRD patterns is not possible, and as indexed, the three diffraction peaks of (*hk*0) can certainly be used to identify the *a* and *b* lattice lengths. It should be noted, however, that as none of the peaks involve a reflection along the *z*-axis, the *c* lattice length cannot be identified from these data – so it is a bit premature to assume a true tetragonal structure. In fact, if the structure really is a tetragonal *I4cm*, then these three peaks cannot be labelled so simply, as multiple reflections fall within the width of each peak: The first is a combination of the (110) and (002) reflections, the second a combination of the (220) and (004) reflections, and the third a combination of the (310), (114), and (222) reflections.²⁴ Due to the evident disorder in the crystal structures of perovskites prepared for photovoltaic applications (i.e. lack of a complete set of diffraction peaks in the XRD pattern), the simple label for these reflections is probably accurate, as if there are substantial reflections from directions (*hkl*) with *l* ≠ 0, additional reflections should be visible in the XRD pattern. In addition, XRD is only sensitive to long range order, information such as local defects or distortions in the crystals can be easily overlooked.

On the other hand, XPS is an element-specific spectroscopic technique, and is used to probe the oxidation states. However, due to the limited electron escape depth, the information obtained from XPS is only from the sample surface. Utilizing a hard X-ray source could improve the bulk sensitivity of the spectra, however, the probing depth is still limited to several tens of nanometres.^{8,25} For devices, the perovskite layer usually has a thickness of a few hundred nanometres, so it is still considered as a surface probe.

In this paper, we inspect the electronic structure of $\text{CH}_3\text{NH}_3\text{PbI}_{3-x}\text{Cl}_x$ using X-ray absorption fine structure (XAFS). It is a local structural probe, by monitoring the interference between incoming and outgoing electrons across the absorption threshold of element of interest. Without the restraint of long range order, XAFS can provide information on chemical environment of the chosen element, such as oxidation states, coordination number, and bond distance. In addition, the X-ray fluorescence detection modes have a much deeper probing depth (i.e. several microns),²⁶ which is sufficient for bulk property detection. We investigate $\text{CH}_3\text{NH}_3\text{PbI}_{3-x}\text{Cl}_x$ films made according to the common recipe using $\text{CH}_3\text{NH}_3\text{I}$ and PbCl_2 as precursors. Four different I/Cl ratios were comparatively studied, including the “magic” ratio 3:1. The local environment of Pb was examined by measuring Pb L_3 -edge (Pb $2p_{3/2}$ core electron to *nd* unoccupied states). A

connection between I/Cl ratio on device performance and the perovskite structure is established.

Experimental

Materials and Characterization

PbCl_2 (99.999%), hydroiodic acid (57% in water) and *N,N*-dimethylformamide (DMF) (anhydrous, amine free; 99.9%) were purchased from Alfa-Aesar. Methylamine (33% in absolute ethanol) was purchased from Sigma-Aldrich. Ethanol (HPLC grade) were purchased from J & K Chemical. PCBM and PEDOT:PSS (CLEVIOS AI 4083) were purchased from Solenne and Heraeus. All materials were used as received.

To prepare the $\text{CH}_3\text{NH}_3\text{PbI}_{3-x}\text{Cl}_x$ precursor solution, $\text{CH}_3\text{NH}_3\text{I}$ was synthesized according to the literature.³ $\text{CH}_3\text{NH}_3\text{I}$ and PbCl_2 powder were mixed in anhydrous DMF with molar ratios of 2.64:1, 2.83:1, 3.00:1, 3.17:1, respectively. The perovskite precursor solution was stirred at 70°C for dissolution and filtered through PTFE filters (0.45 μm) before use.

The $\text{CH}_3\text{NH}_3\text{PbI}_{3-x}\text{Cl}_x$ films were prepared by one-step spin-coating method. The precursor solution was spin-coated on ITO/PEDOT:PSS (40 nm) substrate at 3000 r.p.m for 40 s. The as-prepared films were then annealed on a hot plate at 100°C for ~ 20min.

The morphologies of the films were characterized using a field emission scanning electron microscope (FEI Quanta 200). The thickness of the film was measured using an Ambio Technology XP-200 profilometer. All films investigated here have perovskite layers of thicknesses of around 300 nm. XRF measurement was conducted using a PANalytical (Empyrean) equipment using Cu $K\alpha$ as the excitation source. A layer of poly(methylmethacrylate) (PMMA) was spin-coated on top of the perovskite films prior to the measurement to prevent the films from degradation by humidity. XAFS measurement at the Pb L_3 -edge was performed at the Shanghai Synchrotron Radiation Facility (SSRF), beamline 14W1. Samples were prepared the same way as the ones for XRD measurements. XAFS spectra were collected in X-ray fluorescence mode using a Lytle detector. The photon energy was calibrated using a Pb foil. All spectra were background subtracted and normalized into the incident photon flux.

XAFS data processing and simulation

An XAFS spectrum is usually divided into two parts and analysed separately: X-ray absorption near-edge structure (XANES) refers to spectrum from a few eV below to ~50 eV above the absorption threshold, and beyond that is referred to as extended X-ray absorption fine structure (EXAFS). The XANES and EXAFS spectra were processed using the IFFEFIT software package according to the standard procedure.²⁷ The EXAFS function $\chi(k)$, was obtained by subtracting the post-edge background from the edge-jump normalized absorption spectrum. The EXAFS fitting was performed with IFFEFIT over a *k*-range of 2.5 to 8.5, and an *R*-range between 2.0 and 5.0. All fits were performed in *R*-space with a *k*-weight of 1.

EXAFS fitting was also performed over a variety of k -ranges starting from 2.0 and extended to 10.0, with k -weighting varying from 1.0 to 3.0. Those results are very similar to the ones we report here; however the ones reported here exhibit the best fitting figures of merit.

The EXAFS fitting was done according to the following procedure: a first shell fit to a single iodine atom at 3.2 Å was performed. The resulting E_0 values for all data were averaged, and Athena²⁸ was used to refit the background using the new E_0 values. Then the data were fit again, with E_0 constrained to 0.0 eV.

Each data set was then fit with 3 shells:

1. An inner shell around 2.9 Å, with a fitted coordination number N_1 , fitted Debye-Waller factor σ^2_1 , and fitted bond length Δr_1 .
2. The main iodine shell around 3.2 Å, with a fixed coordination number of $N_2 = 4.0$, and a fitted Debye-Waller factor σ^2_2 , and fitted bond length Δr_2 .
3. An outer shell around 4.0 Å, with a fitted coordination number N_3 , fitted Debye-Waller factor σ^2_3 , and fitted bond length Δr_3 .

All paths involved the same fitted amplitude reduction factor, S_0^2 , for a total of 9 fitted variables. Carbon, nitrogen, oxygen, chlorine, and iodine were all tested as the atomic species for the inner and outer shells for all data sets. Unphysical (negative) values of N_i and/or σ^2_i were discarded. The reported margins of error in the calculated parameters were obtained by refitting the data holding all parameters fixed at their optimum values except for the parameter in question.

XANES spectra for model compounds were calculated using the FDMNES package.²⁹ A broad spectrum ranging from 30 eV below the absorption edge to 150 eV above the edge was calculated using Green's functions, and then the near-edge from -10 eV to 40 eV was calculated using the more accurate finite difference method. The start and end points from the spectrum calculated using the finite difference method fit smoothly within the more extended spectrum calculated using Green's functions. The model compounds were based on the experimentally-determined β -phase of $\text{CH}_3\text{NH}_3\text{PbI}_3$,²⁴ however these compounds included three types of defects next to the absorbing Pb: One or two iodine vacancies, one or two chlorine atoms substituting for iodine, and the CH_3 -end of the CH_3NH_3 molecule moved within 2.9 Å from the absorbing Pb.

Device Fabrication and Measurement

Glass substrate coated with patterned indium tin oxide (ITO) with a sheet resistance of $\sim 10 \Omega \text{ sq}^{-1}$ was cleaned with detergent, ultrasonicated in acetone and ethanol, and then blow dried by nitrogen. Subsequently, the substrates were treated by ultraviolet ozone plasma for 15 min. PEDOT:PSS were spin-coated onto the substrates at 4000 r.p.m. for 60 s. After baked at 140 °C for 20 min, the substrates were transferred into a glovebox for absorbing layer coating and electrode deposition. A 40 wt.% $\text{CH}_3\text{NH}_3\text{PbI}_{3-x}\text{Cl}_x$ precursor solution was spin-coated at 3000 r.p.m. for 40 s. After laid at the petri dish at room temperature for ~ 15 min, the perovskite

films were annealed on a hot plate at 100 °C for ~ 20 min, allowing the color of the films to convert into dark brown. PCBM layers were deposited from a 30 mg/mL chlorobenzene solution at 2000 r.p.m. Subsequently, the ZnO layers were formed by spin-coating a colloidal ZnO nanocrystal solution (1 mg/mL in ethanol) at 3000 r.p.m. for 40 s. Finally, 150-nm thick Al was evaporated through a shadow mask under 10^{-6} Torr (Mini spectra, Kurt J. Lesker). The area of each device was 7.25 mm² determined by a shadow mask.

Device characteristics, current density-voltage (J-V) curves, were measured in a glovebox under a Newport 94023A solar simulator equipped with a 300 W Xenon lamp and an air mass (AM) 1.5G filter was used to generate simulated AM 1.5G solar spectrum irradiation source. The irradiation intensity was 100 mW/cm² calibrated by a Newport standard silicon solar cell 91150.

Results and Discussion

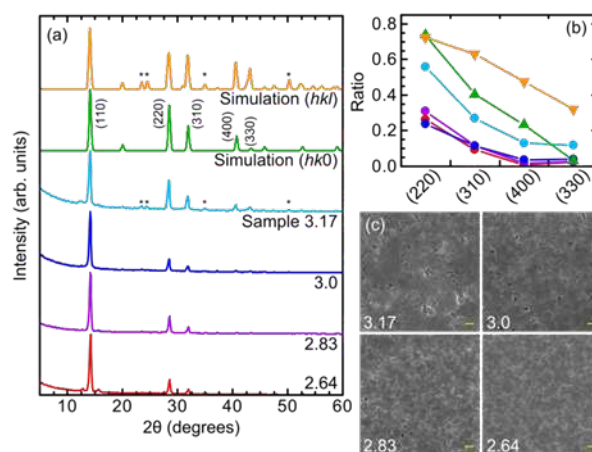


Fig. 1 (a) XRD patterns from the $\text{CH}_3\text{NH}_3\text{PbI}_{3-x}\text{Cl}_x$ films, along with the simulated XRD patterns from the β -phase of $\text{CH}_3\text{NH}_3\text{PbI}_3$ with (hkl) and without $(hk0)$ reflections along the l direction. The * marks the diffraction peaks of (hkl) with $l \neq 0$. (b) the intensity ratios of the labelled peaks in the measured and simulated XRD patterns with respect to the (110) peak. The colours in (b) are consistent with (a). (c) the SEM images from the four films, the scale bar is 1 μm .

The XRD patterns of the four $\text{CH}_3\text{NH}_3\text{PbI}_{3-x}\text{Cl}_x$ films are shown in Fig. 1(a). All films clearly exhibit three main diffractions, which are typically indexed as the (110), (220) and (310) peaks of a tetragonal lattice, as is common for perovskite films prepared for photovoltaics.^{17,21} In the XRD patterns from our data, additional reflection peaks corresponding to (400) and (330) can be identified upon close inspection, although they are much weaker than the main three. These peaks are all at essentially the same angles as the reflections simulated from the ideal $I4cm$ structure, as shown in Fig. 1(a). The XRD pattern from the film prepared with a 3.17:1 ratio of $\text{CH}_3\text{NH}_3\text{I}$ to PbCl_2 ("sample 3.17") also exhibits weak but unambiguous peaks that correspond to reflections in (hkl) with $l \neq 0$; indicated with asterisk marks in Fig. 1(a). Note that the simulated pattern obtained by retaining only the $(hk0)$ reflections from the $I4cm$

structure shown in Fig. 1(a) lacks those peaks, as do the XRD patterns from samples 3.0, 2.83, and 2.64.

The ratio of the total intensities of the reflection peaks labelled (220), (310), (400), and (330) with respect to the total intensity of the peak labelled (110) is shown in Fig. 1(b) for all samples as well as the two simulated patterns. Note that the intensity ratios for samples 3.0, 2.83, and 2.64 are essentially the same, while that of 3.17 is closer to the simulations. In the full $I4cm$ structure peak (330) is actually an overlap of (314), (402), and (330) reflections, so the relatively large intensity of the peak labelled “(330)” in sample 3.17 is another indication of order along the c -axis.

SEM images of the four films are shown in Fig. 1(c). All films exhibit similar morphologies with comparable grain sizes, so morphology effect on the properties of the perovskites is not the major issue. According to the XRD data discussed above, we see that samples 2.64, 2.83, and 3.0 all have planar order, with a, b lattice lengths essentially the same as those previously reported,²⁴ but only sample 3.17 has a true tetragonal structure with order along the c -axis. To gain further insight into the local order of these samples we turn to our EXAFS measurements.

Our first shell fitting using Pb coordinated by 6 iodine atoms in an octahedral arrangement is shown in Figure 2. The fitted parameters for all four samples are all very similar, as the amplitude reduction factors S_0^2 , the Debye-Waller factors σ^2 , and the shifts in Pb-I the bond length for all four samples all fall within the error bounds of each other. We obtain an average amplitude reduction factor of $S_0^2 = 0.86 \pm 0.08$, an average Debye-Waller factor of $\sigma^2 = 0.020 \pm 0.002 \text{ \AA}^2$, and an average Pb-I bond length of $3.171 \pm 0.005 \text{ \AA}$. The latter is reasonably close to the a, b -planar Pb-I bond length of $3.1611 \pm 0.0015 \text{ \AA}$ in tetragonal $\text{CH}_3\text{NH}_3\text{PbI}_3$.²⁴ The fitted parameters for each sample are reported in Table 1. We note, however, that there is an intriguing trend in the “effective coordination number” NS_0^2 , as this value decreases as the molar ratio of $\text{CH}_3\text{NH}_3\text{I}$ to PbCl_2 increases.

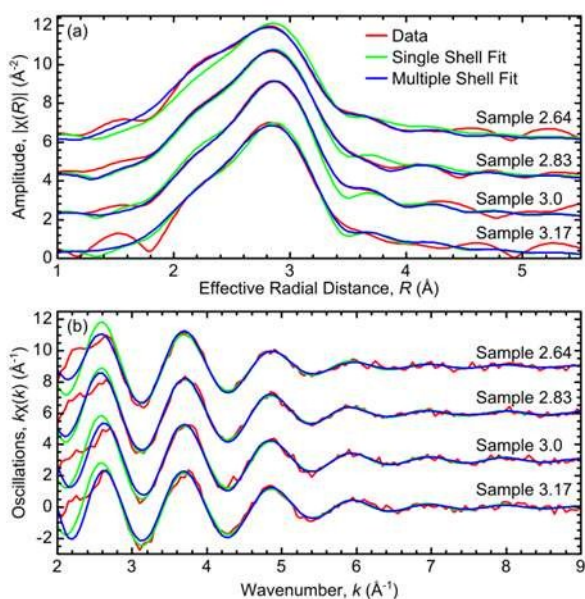


Fig. 2 EXAFS spectra and fits in (a) R -space and (b) k -space for all samples.

Although the parameters obtained from these fits are all reasonable, the fits themselves leave something to be desired, as they noticeably deviated from our data at low and high k . For this reason we have employed a three-shell fitting model, as described above, to examine the possibility that there are defects at smaller or larger distances from the Pb absorbing atom.

Table 1. Parameters obtained from fitting the Pb L3 EXAFS with scattering from a single coordination shell of iodine.

Sample	Amplitude, NS_0^2	Debye-Waller Factor, $\sigma^2 (\text{\AA}^2)$	Bond Length, $r (\text{\AA})$	R-factor of fit
2.64	5.4 ± 0.5	0.023 ± 0.003	3.173 ± 0.006	0.013
2.83	5.3 ± 0.4	0.020 ± 0.002	3.173 ± 0.004	0.009
3.0	5.0 ± 0.5	0.017 ± 0.002	3.170 ± 0.005	0.014
3.17	5.0 ± 0.5	0.018 ± 0.002	3.169 ± 0.006	0.014

The multiple-shell EXAFS fits, also shown in Fig. 2, are all in much better agreement with the measured data than the single-shell EXAFS fit, as the R-factors of the multiple-shell fits are an order of magnitude lower than those of the single-shell fits. The results should be examined with care, as each fit involved 9 degrees of freedom which approaches the Nyquist limit for the data (11 independent points, based on the k - and R -ranges for the fit). However, as noted above, we performed fitting over a wide variety of k - and R -ranges, and almost all of these fits produced similar results to the ones shown here. The optimum values for the parameters from the multiple-shell fits are shown in Table 2. We will describe the results from the model here but suppress the full number of significant figures and the error bars for brevity. The coordination numbers are estimated by assuming that the amplitude reduction factor S_0^2 is the same for all compounds, and that sample 3.17 possesses Pb fully coordinated with 6 I (Sample 3.17 exhibited the highest NS_0^2 value, and recall that N_2 was assumed to be present during the fit). The assumption that sample 3.17 is fully coordinated is justified by the tetragonal structure exhibited in the XRD pattern. Furthermore, while we cannot conclusively prove that sample 3.17 is fully coordinated, the trend in coordination numbers between the different coordination shells and the different samples is accurate. If, for example, the true coordination number of Pb in sample 3.17 were 5.8 instead of 6 (as assumed here), then all coordination numbers for all samples reported herein should be rescaled by a factor of 5.8/6.0.

Table 2. Parameters obtained from fitting the Pb L₃ EXAFS with scattering from three coordination shells. For the first and third shells, we tried carbon, nitrogen, oxygen, chlorine, and iodine as the scattering atoms, only the best, physical results are shown here.

Parameter	Sample 2.64	Sample 2.83	Sample 3.0	Sample 3.17
First Shell	Chlorine	Chlorine	Carbon	Carbon
N ₁	1.8 ± 0.2	0.26 ± 0.07	0.35 ± 0.06	0.67 ± 0.07
σ ₁ ² (Å ²)	0.042 ± 0.002	0.032 ± 0.007	0.015 ± 0.005	0.030 ± 0.004
r ₁ (Å)	2.867 ± 0.002	3.00 ± 0.03	2.89 ± 0.02	2.90 ± 0.02
Second Shell	Iodine	Iodine	Iodine	Iodine
N ₂	3.7 ± 0.1	4.7 ± 0.1	4.9 ± 0.1	6 ± 0.1
σ ₂ ² (Å ²)	0.020 ± 0.001	0.020 ± 0.001	0.019 ± 0.001	0.023 ± 0.001
r ₂ (Å)	3.167 ± 0.002	3.173 ± 0.002	3.167 ± 0.002	3.163 ± 0.002
Third Shell	Carbon	Iodine	Nitrogen	Carbon/Nitrogen
N ₃	0.9 ± 0.2	0.23 ± 0.04	0.50 ± 0.06	< 10 ⁻⁴
σ ₃ ² (Å ²)	0.006 ± 0.006	0.003 ± 0.002	0.007 ± 0.005	-
r ₃ (Å)	4.22 ± 0.03	3.86 ± 0.02	4.17 ± 0.02	-
R-factor	0.00284	0.00205	0.00279	0.00430

For sample 2.64, the model suggests that Pb is coordinated by 3.7 I with a bond length of 3.17 Å, and 1.8 Cl atoms with a bond length of 2.87 Å. The latter bond length is quite close to that of 2.85 Å in PbCl₂.³⁰ For sample 2.83, the model suggests that Pb is coordinated by 4.7 I (at 3.17 Å) and 0.3 Cl (at 3.0 Å) atoms. Recall that we tried using C, O, N, Cl, and I as the nearer scattering site and for both measurements Cl proved the best fit. These models also support the chemistry discussed in the introduction. As more CH₃NH₃I is added, more Cl is removed from the perovskite structure. The lowest ratio of CH₃NH₃I to PbCl₂, 2.64, still features Pb that are coordinated by an average of almost 2 Cl atoms, while increasing the ratio to 2.83 reduces the Cl coordination to only 0.3. Note, however, that the total coordination of Pb is reduced from 5.5 to 5.0 as the CH₃NH₃I to PbCl₂ ratio increases from 2.64 to 2.83, suggesting a substantial amount of I vacancies are present. The third shell for sample 2.64 is from 0.9 C atoms at a distance of 4.22 Å; a reasonable distance for the CH₃-end of a CH₃NH₃ molecule, while the third shell for sample 2.83 is from 0.2 I atoms at a distance of 3.86 Å.

For sample 3.0, the model suggests that Pb is coordinated by 4.9 I with a bond length of 3.17 Å. There is around 0.3 C present even closer to Pb at a bond length of 2.89 Å, and a further 0.5 N at a distance of 4.17 Å from the Pb. Note again that Pb lacks a full 6-halide coordination shell; this appears to be partially corrected by the proximity of the CH₃-end of a CH₃NH₃ molecule. The more distance N may be the NH₃-end of a CH₃NH₃ molecule attracted to a different Pb site, or from a CH₃NH₃ slightly off-centre in a perovskite cell.

In these three samples, our EXAFS model suggests that our notion of an approximately octahedral PbI₆ structure in perfect CH₃NH₃PbI₃ should be replaced by a well-defined PbI₄ planar structure in the *ab* lattice plane, with more irregular bonding along the *c*-axis, consisting of Cl, I, and halide vacancies. This picture is supported by the XRD patterns from these three samples, which again exhibit well-defined scattering peaks that can be indexed by reflections in (*hk*0) only. Incidentally, since this picture suggests a substantial amount of halide vacancies,

one should not assume that these samples contain the stoichiometric amount of CH₃NH₃, either.

Our EXAFS model also suggests a very rapid decrease in I content over a relatively narrow increase in the CH₃NH₃I:PbCl₂ ratio (from 2.64 to 2.83). One possible explanation can be reached by considering the perovskite structure and the Pb-Cl and Pb-I bond lengths. If we assume that a PbI₄ planar structure forms, as discussed above, any remaining Cl must occupy the halide sites along the *c*-axis, as will any additional I. However the Pb-Cl bond length is much shorter than the Pb-I bond length (refer back to Table 2), therefore the co-existence of a large fraction of both Cl and I on these sites would induce an immense amount of strain on the lattice. As the CH₃NH₃I:PbCl₂ ratio is increased, we therefore expect there to be a tipping point where a perovskite dominated by Cl occupying the *c*-axis sites (as we have with sample 2.64) rapidly changes to a perovskite dominated by I occupying the *c*-axis sites (as we have with all remaining samples). We note that an attempt to form a perovskite from a 1:1 ratio of CH₃NH₃Cl and PbI₂ resulted in separate CH₃NH₃PbCl₃ and PbI₂ phases, with relatively little CH₃NH₃Pb_{1-x}Cl_x perovskite formed, with 0.12.¹³

For sample 3.17, on the other hand, we have 0.7 C at a bond length of 2.9 Å from Pb, and 6 I at 3.17 Å. We again stress that we assumed that sample 3.17 possessed a full coordination of 6 I, because it exhibited the highest N₂S₀² value from all samples. It may be possible that sample 3.17 has *overcoordinated* Pb, although this seems unlikely from a structural point of view given the XRD pattern, but if sample 3.17 is *undercoordinated*, then all of the coordination numbers reported above should be reduced by the same fraction. The third coordination sphere of sample 3.17 has a negligible coordination number. This is also an indication of good perovskite crystal structure, since the CH₃NH₃ in a perovskite should be at least 4.7 Å from the Pb site (assuming the CH₃NH₃ are aligned with the body diagonal, otherwise the distance will be even greater). The closer 0.7 C at 2.9 Å from Pb is very similar to that in the sample 3.0, and may suggest that some Pb²⁺ sites can form stereoactive lone-pairs, which attract the CH₃-end of CH₃NH₃ through hydrogen bonding. In the defect heavy sample 3.0, this could lead to CH₃NH₃ occupying an iodine vacancy site; consequently leading to the N-coordination at 4.17 Å; while in the sample 3.17, without a substantial amount of I vacancies, the CH₃NH₃ is confined to the perovskite cage with the NH₃-end of the molecule well beyond 5 Å from any Pb site.

Our EXAFS fitting suggests a wide range of environments for Pb sites in our perovskite samples, including Pb coordinated with up to 2 Cl, Pb with I vacancies, and Pb with the CH₃-end of CH₃NH₃ less than 3 Å away. Several of these structures are shown in Fig. 3(a). In principle, one should be able to use the Pb L₃ XANES to study the chemical environment of Pb as well; however in our case the Pb L₃ XANES from all samples are essentially identical, as shown in Fig. 3(b). The simulated Pb L₃ XANES from the structures shown in Fig. 3(a), shown in Fig. 3(b), illustrate why: Within the resolution of the Pb L₃ XANES measurement all of the structures exhibit virtually identical

spectra. This unfortunate situation limits the utility of Pb L₃ XANES in determining the chemical environment of perovskites.

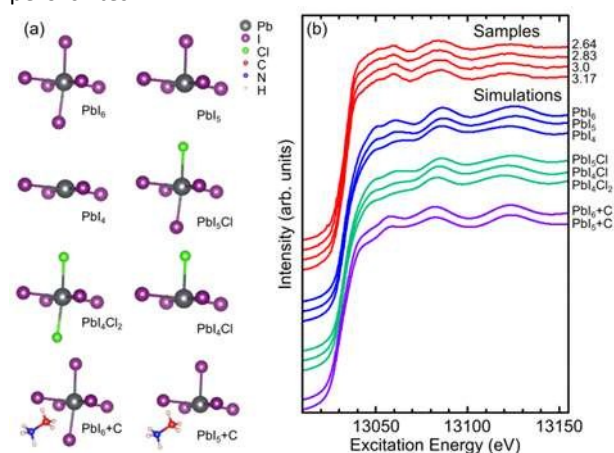


Fig. 3 (a) Structures of Pb coordinated by I, Cl, and nearby CH₃NH₃. All of these structures were formed from a tetragonal perovskite lattice (the PbI₆ cluster is the perovskite, all others are perovskites with various defects), but for clarity only elements within 4 Å of the absorbing Pb site are shown. (b) Pb L₃ XANES from the samples and simulated using the structures in (a).

Finally, we fabricated solar cells incorporating these perovskite films and examined their performance. The J-V curve is shown in Fig. 4(a), and the detailed parameters are listed in Table 3. We note that our devices did not show significant hysteresis in their J-V curves measured with forwards and backwards voltage sweep between the scan rates of 0.063 V/s and 0.73 V/s. The values listed were based on 5 sets of devices for each ratio. The variation of I/Cl ratio causes no significant effect on the V_{OC}, which is not surprising, since the electronic structure of perovskite is not altered. However, it leads to a direct impact on the J_{SC}: it increases as I/Cl ratio grows, but once the ratio is above 3:1, a significant drop occurs. The peak power conversion efficiency (PCE) was indeed achieved using the perovskite of I/Cl precursor ratio of 3:1.

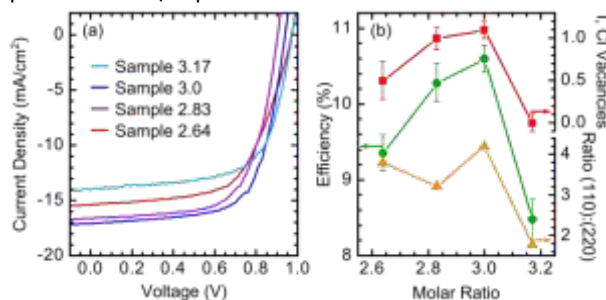


Fig. 4 (a) J-V curves for the four samples with different CH₃NH₃/PbCl₂ ratio under light at simulated AM 1.5 solar illumination at 100 mW cm⁻², measured with a scan rate of 0.73 V/s. (b) The PCEs of the devices (green), the number of halide vacancies from EXAFS fitting (red), and ratio of the (110) peak intensity to the (220) peak intensity from the XRD patterns (yellow) as a function of the ratio of CH₃NH₃ to PbCl₂.

Table 3. Electrical output characteristics of the devices with perovskite films with different CH₃NH₃/PbCl₂ ratios under light at stimulated AM 1.5 solar illumination at 100 mW cm⁻². V_{OC}: open circuit voltage, J_{SC}: short circuit current density, FF: fill factor.

CH ₃ NH ₃ /PbCl ₂	V _{OC} (V)	J _{SC} (mA/cm ²)	FF	η (%)
2.64:1	0.96 ± 0.01	15.35 ± 0.23	0.64 ± 0.03	9.35 ± 0.2
2.83:1	0.90 ± 0.01	16.60 ± 0.18	0.69 ± 0.02	10.27 ± 0.25
3.00:1	0.94 ± 0.01	17.07 ± 0.26	0.67 ± 0.01	10.59 ± 0.18
3.17:1	0.96 ± 0.01	13.96 ± 0.64	0.61 ± 0.03	8.47 ± 0.27

The trend in the PCEs of these devices actually mirrors the number of halide (I or Cl) vacancies found from EXAFS fitting (i.e. the fitted Cl + I coordination number subtracted from 6), and apart from sample 2.64, it also mirrors the ratio of the intensity of the (110) peak to the intensity of the (220) peak in the XRD patterns.

Our XRD and EXAFS data suggest that forming a tetragonal perovskite that is well-ordered along the c-axis as well as in the a,b-plane requires an excess of iodine, as the natural perovskite formed from PbCl₂ tends to exhibit iodine vacancies, even after the Cl is completely removed. Comparing these findings to the device data, we see that a well-ordered tetragonal perovskite may *not* be the best structure for good device performance, and iodine vacancies may be necessary for good charge transport. Indeed, previous studies have highlighted that iodine vacancies may act as acceptor levels or facilitate ionic transport, both of which would influence photovoltaic performance.^{31,32} On the other hand, residual chlorine is also not conducive to good photovoltaic performance; as the stronger chemical interactions of chlorine compared to iodine could lead to deep trap states.

Conclusions

To summarize, we have studied the crystal structure of CH₃NH₃PbI_{3-x}Cl_x formed from CH₃NH₃I and PbCl₂ precursors with molar ratios of 2.64:1, 2.83:1, 3.0: and 3.17:1 with XRD and Pb L₃-edge XAFS. We find that only the XRD pattern from the CH₃NH₃PbI_{3-x}Cl_x film formed with a 3.17:1 ratio of CH₃NH₃ to PbCl₂ clearly exhibits ordered domains that grow along the c-axis of a tetragonal perovskite crystal structure. The other three films exhibit good crystalline order in the a,b-plane, but no XRD peaks involving reflections along the c-axis are visible. A previous study found CH₃NH₃PbI_{3-x}Cl_x films (3:1 ratio) exhibited preferential growth on a micron scale, while pure CH₃NH₃PbI₃ did not,³⁴ reflecting the possibility that several of our samples do not exhibit reflections in the c-axis because they have long-range single-crystalline order therein. However, we should also note that the surface morphology of the CH₃NH₃PbI_{3-x}Cl_x films discussed in Reference 34 exhibit clear needle-like crystallites 2-3 μm long, while our films are rather flat. Further study will be needed to precisely define the difference in the long-range crystalline order in these films; for the present it is sufficient to note that only sample 3.17 exhibits diffraction peaks indicative of reflections partially along the c-axis.

By fitting the Pb L₃-edge EXAFS spectra with a 3-shell model, we find that sample 3.17 has the highest Pb-I coordination,

which we have assumed herein to be 6 (If the true coordination number is different, then all other coordination numbers for all samples should be rescaled appropriately). The other samples have iodine vacancies and may even have chlorine present at low molar ratios. These vacancies may explain the lack of crystalline order along the c-axis. The number of halide vacancies per Pb site follows the same trend as the device PCE as a function of the $\text{CH}_3\text{NH}_3\text{I}$ to PbCl_2 molar ratio. The fact that the most crystalline device; that formed from a 3.17:1 molar ratio, has the poorest PCE suggests that iodine ionic transport, facilitated by iodine vacancies, is beneficial to device performance. On the other hand, the PCE also declines with increased Cl content, suggesting that Cl may be responsible for deep charge traps. It has previously been suggested that growing $\text{CH}_3\text{NH}_3\text{PbI}_3$ in I-poor conditions reduces the formation of deep traps associated with I substituting for Pb,³⁵ however our findings suggest that obtaining I-poor growth conditions by making the precursors Cl-rich is not a viable strategy, as traps associated with Cl become dominant.

In closing, we would also like to point out that $\text{CH}_3\text{NH}_3\text{PbI}_{3-x}\text{Cl}_x$ films synthesized with $\text{CH}_3\text{NH}_3\text{I}:\text{PbCl}_2$ ratios of less than 3:1 would be an interesting platform to study the direct influence of Cl on the electronic structure of these materials. All previous experimental studies that we are aware of have focused on only the 3:1 ratio, which has negligible Cl content (as previously verified, and as suggested by our EXAFS modelling).^{8,33,36} Although films with lower ratios have lower PCEs, they still exhibit many of the same structural and electronic properties as the ideal 3:1 perovskites. Tailoring the molar ratio may therefore provide a means of controlling the types of defects present in the perovskite, and therefore provide a rich platform for identifying the specific influence each form of defect has on the photovoltaic properties.

Acknowledgements

This work is funded by the National Natural Science Foundation of China (NSFC) project number U1432106, and the National Basic Research Program of China (973 Program) project number 2012CB932402. The authors acknowledge the support from Soochow University-Western University Center for Synchrotron Radiation Research and Collaborative Innovation Center of Suzhou Nano Science and Technology (NANO-CIC), Soochow University.

References

- 1 A. Kojima, K. Teshima, Y. Shirai and T. Miyasaka, *J. Am. Chem. Soc.*, 2009, **131**, 6050-6051.
- 2 D. Liu and T. L. Kelly, *Nat. Photonics*, 2013, **8**, 133-138.
- 3 M. M. Lee, J. Teuscher, T. Miyasaka, T. N. Murakami and H. J. Snaith, *Science*, 2012, **338**, 643-647.
- 4 S. D. Stranks, G. E. Eperon, G. Grancini, C. Menelaou, M. J. Alcocer, T. Leijtens, L. M. Herz, A. Petrozza and H. J. Snaith, *Science*, 2013, **342**, 341-344.
- 5 E. Edri, S. Kirmayer, A. Henning, S. Mukhopadhyay, K. Gartsman, Y. Rosenwaks, G. Hodes and D. Cahen, *Nano Lett.*, 2014, **14**, 1000-1004.
- 6 J. M. Ball, M. M. Lee, A. Hey and H. J. Snaith, *Energ. Environ. Sci.*, 2013, **6**, 1739.
- 7 G. E. Eperon, V. M. Burlakov, P. Docampo, A. Goriely and H. J. Snaith, *Adv. Funct. Mater.*, 2014, **24**, 151-157.
- 8 B. Philippe, B.-W. Park, R. Lindblad, J. Oscarsson, S. Ahmad, E. M. J. Johansson and H. Rensmo, *Chem. Mater.*, 2015, **27**, 1720-1731.
- 9 Q. Chen, H. Zhou, Y. Fang, A. Z. Stieg, T. B. Song, H. H. Wang, X. Xu, Y. Liu, S. Lu, J. You, P. Sun, J. McKay, M. S. Goorsky and Y. Yang, *Nat. Commun.*, 2015, **6**, 7269.
- 10 J. You, Z. Hong, Y. Yang, Q. Chen, M. Cai, T.-B. Song, C.-L. Chen, S. Lu, Y. Liu, H. Zhou and Y. Yang, *ACS Nano*, 2014, **8**, 1674-1680.
- 11 G. Grancini, S. Marras, M. Prato, C. Giannini, C. Quarti, F. De Angelis, M. De Bastiani, G. E. Eperon, H. J. Snaith, L. Mannella and A. Petrozza, *J. Phys. Chem. Lett.*, 2014, **5**, 3836-3842.
- 12 S. Colella, E. Mosconi, G. Pellegrino, A. Alberti, V. L. P. Guerra, S. Masi, A. Listorti, A. Rizzo, G. G. Condorelli, F. De Angelis and G. Gigli, *J. Phys. Chem. Lett.*, 2014, **5**, 3532-3538.
- 13 S. Colella, E. Mosconi, P. Fedeli, A. Listorti, F. Gazzera, S. Orlandi, P. Ferro, T. Besagni, A. Rizzo, G. Calestani, G. Gigli, F. De Angelis and R. Mosca, *Chem. Mater.*, 2013, **25**, 4618-4618.
- 14 E. L. Unger, A. R. Bowring, C. J. Tassone, V. L. Pool, A. Gold-Parker, R. Cheacharoen, K. H. Stone, E. T. Hoke, M. F. Toney and M. D. McGehee, *Chem. Mater.*, 2014, **26**, 7158-7165.
- 15 S. T. Williams, F. Zuo, C. C. Chueh, C. Y. Liao, P. W. Liang and A. K. Jen, *ACS Nano*, 2014, **8**, 10640-10654.
- 16 H. Yu, F. Wang, F. Xie, W. Li, J. Chen and N. Zhao, *Adv. Funct. Mater.*, 2014, **24**, 7102-7108.
- 17 E. Edri, S. Kirmayer, M. Kulbak, G. Hodes and D. Cahen, *J. Phys. Chem. Lett.*, 2014, **5**, 429-433.
- 18 J. H. Noh, S. H. Im, J. H. Heo, T. N. Mandal and S. I. Seok, *Nano Lett.*, 2013, **13**, 1764-1769.
- 19 E. Mosconi, A. Amat, M. K. Nazeeruddin, M. Grätzel and F. De Angelis, *J. Phys. Chem. C*, 2013, **117**, 13902-13913.
- 20 A. Dualeh, N. Tétreault, T. Moehl, P. Gao, M. K. Nazeeruddin and M. Grätzel, *Adv. Funct. Mater.*, 2014, **24**, 3250-3258.
- 21 D. Wang, Z. Liu, Z. Zhou, H. Zhu, Y. Zhou, C. Huang, Z. Wang, H. Xu, Y. Jin, B. Fan, S. Pang and G. Cui, *Chem. Mater.*, 2014, **26**, 7145-7150.
- 22 C. W. Chen, H. W. Kang, S. Y. Hsiao, P. F. Yang, K. M. Chiang and H. W. Lin, *Adv. Mater.*, 2014, **26**, 6647-6652.
- 23 D. Shi, V. Adinolfi, R. Comin, M. Yuan, E. Alarousu, A. Buin, Y. Chen, S. Hoogland, A. Rothenberger, K. Katsiev, Y. Losovyj, X. Zhang, P. A. Dowben, O. F. Mohammed, E. H. Sargent and C. M. Bakr, *Science*, 2015, **347**, 519-522.
- 24 C. C. Stoumpos, C. D. Malliakas and M. G. Kanatzidis, *Inorg. Chem.*, 2013, **52**, 9019-9038.
- 25 R. Lindblad, D. Bi, B.-W. Park, J. Oscarsson, M. Gorgoi, H. Siegbahn, M. Odellius, E. M. J. Johansson and H. Rensmo, *J. Phys. Chem. Lett.*, 2014, **5**, 648-653.
- 26 The specific X-ray probing depth of a given material can be calculated from the attenuation length, which is available at http://henke.lbl.gov/optical_constants/
- 27 M. Newville, *J. Synchrotron Rad.*, 2001, **8**, 322-324.
- 28 B. Ravel and M. Newville, *J. Synchrotron Rad.*, 2005, **12**, 531-541.
- 29 Y. Joly, *Phys. Rev. B*, 2001, **63**, 125120-125129.
- 30 R. W. G. Wyckoff, *Crystal Structures*, Interscience Publishers, New York, 2 edn., 1963.
- 31 W. J. Yin, T. Shi and Y. Yan, *Appl. Phys. Lett.*, 2014, **105**, 063903.
- 32 C. Eames, J. M. Frost, P. R. F. Barnes, B. C. O'Regan, A. Waihan and M. S. Islam, *Nat. Comm.*, 2015, **6**, 7497.

ARTICLE

Journal Name

- 33 D. E. Starr, G. Sadoughi, E. Handick, R. G. Wilks, J. H. Alsmeyer, L. Kohler, M. Gorgoi, H. J. Snaith, and M. Bar, *Energ. Environ. Sci.*, 2015, **8**, 1609.
- 34 G. Pellegrino, S. Colella, I. Deretzis, G. G. Condorelli, E. Smecca, G. Gigli, A. La Magna, and A. Alberti, *J. Phys. Chem. C*, 2015, **119**, 19808.
- 35 A. Buin, P. Pietsch, J. Xu, O. Voznyy, A. H. Ip, R. Comin, and E. H. Sargent, *Nano Lett.* 2014, **14**, 6281.
- 36 B. Conings, L. Baeten, C. De Dobbelaere, J. D'Haen, J. Manca, and H.-G. Boyen, *Adv. Mater.* 2013, **26**, 2041.

Nanoscale Accepted Manuscript